



Originally published as:

Stefanova Vassileva, M., Motagh, M., Walter, T. R., Wetzel, H.-U., Senyukov, S. L. (2020):
The 29 March 2017 Yuzhno-Ozernovskoe Kamchatka Earthquake: Fault Activity in An
Extension of the East Kamchatka Fault Zone as Constrained by InSAR Observations. -
Bulletin of the Seismological Society of America, 110, 3, 1101-1114.

<https://doi.org/10.1785/0120190174>

Bulletin of the Seismological Society of America

The 29 March 2017 Yuzhno-Ozernovskoe Kamchatka earthquake: fault activity in an extension of the East Kamchatka Fault Zone as constrained by InSAR observations

--Manuscript Draft--

Manuscript Number:	BSSA-D-19-00174R4
Article Type:	Article
Section/Category:	Regular Issue
Full Title:	The 29 March 2017 Yuzhno-Ozernovskoe Kamchatka earthquake: fault activity in an extension of the East Kamchatka Fault Zone as constrained by InSAR observations
Corresponding Author:	Magdalena S. Vassileva German Research Centre for Geosciences Potsdam, Brandenburg GERMANY
Corresponding Author's Institution:	German Research Centre for Geosciences
Corresponding Author E-Mail:	magdalena.stefanova.vassileva@gfz-potsdam.de
Order of Authors:	Magdalena S. Vassileva Mahdi Motagh Thomas R. Walter Hans-Ulrich Wetzel Sergey L. Senyukov
Abstract:	Recent earthquakes offshore of the northeastern Kamchatka coast reveal that this region is seismically active, though details of the locations and complexity of the faulted system are lacking. The northern part of Kamchatka has poor coverage of seismic stations and no coverage of ground geodetic instruments. Here we exploit the Differential Interferometric Synthetic Aperture Radar (DInSAR) technique to characterize the fault geometry and kinematic dynamics associated with the 29 March 2017 Mw 6.6 Yuzhno-Ozernovskoe Kamchatka earthquake. The aim is to contribute to identify the active fault branches and to better understand the complex tectonic regime in this region. D2InSAR technique have been never applied before in Kamchatka Peninsula for co-seismic analysis. We produced coseismic deformation maps using ALOS-II ascending and descending and Sentinel-1 descending SAR interferometric couples, and jointly inverted the three datasets using elastic half-space fault modeling to retrieve the source geometry and slip distribution. Predominant uplift deformation have been detected from both geometries amounting to around 20 cm near the shoreline. The nonlinear inversion suggested a north-west-dipping oblique thrust faulting with right-lateral rupture. We discuss the Yuzhno-Ozernovskoe Kamchatka earthquake in a regional tectonic framework and compare the fault model to the focal mechanisms retrieved by global and regional seismic networks. The model fault geometry is found to be generally consistent with the seismic data, but also reveals that a hitherto unknown fault was ruptured. The identified fault structure is interpreted as the northern extension of the East Kamchatka Fault Zone, implying that the region is more complex than previously thought. Important implications arise for the presence of unknown faults in this area and for similar regions elsewhere.
Author Comments:	Dear Editor, we thank you for your last corrections and suggestions. We applied all of them and we changed the key points as suggested.
Suggested Reviewers:	Roland Burgmann Professor, University of California Berkeley burgmann@seismo.berkeley.edu expert in active tectonics Zhong Lu Professor, Dedman College of Humanities & Sciences zhonglu@smu.edu expert in InSAR imagery and numerical modeling

	<p>Caijun Xu Professor, School of Geodesy and Geomatics cjxu@sgg.whu.edu.cn expert in active crustal deformation processes with GPS & InSAR measurements</p> <p>Cecile Lasserre Researcher, French Geological Survey m.demichelle@brgm.fr expert in neotectonics and geodetic (InSAR and GPS) measurements</p> <p>Marcello De Michele Researcher, French Geological Survey m.demichelle@brgm.fr expert in active tectonics and InSAR measurements</p>
Opposed Reviewers:	
Response to Reviewers:	
Additional Information:	
Question	Response
<p>Key Point #1: Key Points are now mandatory for BSSA, and will appear at the front of articles starting in 2020. Please submit three COMPLETE sentences addressing the following: 1) what problem did you address?; 2) what conclusions did you come to?; and 3) what are the implications of your findings? Each point must be 110 characters or less (including spaces).</p>	<p>We infer fault geometry and slip distribution from DInSAR in the tectonically complex region of Kamchatka.</p>
Key Point #2:	<p>The 2017 M6.6 earthquake ruptured a previously unidentified reverse fault in the Kamchatka fault zone.</p>
Key Point #3:	<p>Results show even more regional complexity, and the utility of DInSAR in areas of sparse seismic coverage.</p>

The 29 March 2017 Yuzhno-Ozernovskoe Kamchatka earthquake: fault activity in an extension of the East Kamchatka Fault Zone as constrained by InSAR observations

Magdalena S. Vassileva¹, Mahdi Motagh¹, Thomas R. Walter², Hans-Ulrich Wetzel¹, Sergey L. Senyukov³

¹German Research Centre for Geosciences, Remote Sensing, Telegrafenberg 34, 14473 Potsdam Germany

²German Research Centre for Geosciences, Physics of Earthquakes and Volcanoes, Helmholtzstraße 6/7, 14467 Potsdam, Germany

³Kamchatkan Branch of Geophysical Survey, Russian Academy of Sciences, Piipa boulevard, 9, 683006 Petropavlovsk-Kamchatskii, Russia

Note: Magdalena S. Vassileva and Mahdi Motagh also at Leibniz University Hannover, Institute of Photogrammetry and GeoInformation, Nienburger Str. 1, 30167 Hannover, Germany; Sergey L. Senyukov also at Schmidt Institute of Physics of the Earth, Russian Academy of Sciences, Bolshaya Gruzinskaya str., 10-1, 123242 Moscow, Russia

Abstract

Recent earthquakes off the north-eastern Kamchatka coast reveal that this region is seismically active, although details of the locations and complexity of the fault system are lacking. The northern part of Kamchatka has poor coverage by permanent seismic stations and ground geodetic instruments. Here, we exploit the differential interferometric synthetic aperture radar

(DInSAR) technique to characterize the fault geometry and kinematic dynamics associated with the 29 March 2017 Mw 6.6 Yuzhno-Ozernovskoe earthquake. The aim is to contribute to identifying the active fault branches and to better understanding the complex tectonic regime in this region using the DInSAR technique, which has never before been applied to the analysis of co-seismic offsets in Kamchatka.

We produced co-seismic deformation maps using Advanced Land Observing Satellite (ALOS)-2 ascending and descending and Sentinel-1A descending SAR scenes and we detected a predominant uplift up to 20 cm and a westward motion of approximately 7 cm near the shoreline. We jointly inverted the three geodetic datasets using elastic half-space fault modelling to retrieve source geometry and fault kinematics. The best fit solution for the nonlinear inversion suggests a north-west-dipping oblique reverse fault with right-lateral rupture.

The model fault geometry is generally consistent with the seismic data but also reveals that a hitherto unknown fault was ruptured. The identified fault structure is interpreted as the northern extension of the East Kamchatka Fault Zone, implying that the region is more complex than previously thought. Important implications arise for the presence of unknown faults at the edges of subduction zones that can generate earthquakes with magnitudes greater than Mw 6.

Keywords: Kamchatka, DInSAR, subduction zone, co-seismic deformation

Introduction

The Kamchatka subduction zone is a consequence of the 77 to 83 mm/yr convergence between the Pacific Plate and Okhotsk microplate, giving rise to mountain-building processes, active volcanoes and high tectonic seismicity (Bürgmann et al., 2005; DeMets et al., 1990). Some of the

historical earthquakes have reached a moment magnitude of 9, such as in 1952, and more events have reached a moment magnitude of 8, such as in 1904 (M_s 8), 1923 (M_w 8.5) and 1959 (M_w 8.2) (Bürgmann et al., 2005). Moreover, some strong earthquakes occurred inland following the volcanic belt, as in 2003 (M_w 6.9), 2004 (M_w 6.9) and 2016 (M_w 7.2) (data from the Seismological Data Information System of Kamchatka Branch of Geophysical Survey of Russian Academy of Science Earthquakes Catalogue for Kamchatka and the Commander Islands (1962–present), see Data and Resources). Strong earthquakes also occurred off the western Kamchatka coast in 2013 (M_w 8.3) and 2008 (M_w 7.7 and 7.3) and along the Pacific-Aleutian transform boundary in 2003 (M_w 6.7), 2017 (M_w 7.7) and the recent 2018 (M_w 7.2) (data from the Seismological Data Information System of Kamchatka Branch of Geophysical Survey of Russian Academy of Science Earthquakes Catalogue for Kamchatka and the Commander Islands (1962–present), see Data and Resources) (see Fig. 1).

Associated with offshore earthquake activities are also potential tsunami hazards. The proper characterization of the factors that govern seismic energy accumulation and release and the identification of the locations and geometries of possibly seismogenic faults are essential for tsunami hazard assessment (Baer et al., 2008; Scott et al., 2018; Tong et al., 2010). The DInSAR technique has become a standard tool for the detection of co- and post-seismic deformation (Atzori et al., 2009, 2008; Çakir et al., 2003; Motagh et al., 2010, 2007). Despite the availability of proper SAR interferometric pairs across the region, a finite fault model incorporating such data for the 29 March 2017 Yuzhno-Ozernovskoe earthquake has not been produced yet. In this study, we investigate the geometry and fault slip model of the Yuzhno-Ozernovskoe earthquake using both C- and L-band DInSAR measurements. In view of the complex tectonic processes

that take place in this region, we contribute to identifying the active fault branches and provide a tectonic interpretation of the ongoing regional processes.

[Figure 1]

Tectonic background

The Kamchatka Peninsula is located in a tectonically active region and has one of the highest seismic hazard potentials in the world (Gorbatov et al., 1997). The main geographic and geological features and tectonic complexities are illustrated in Figs. 1 and 2 (see also Supplemental Material).

The north-eastern part of the peninsula is located on a triple junction among the Pacific Plate and the Bering Sea and Okhotsk microplates, where a dramatic shift in subduction dynamics occurs (Cook et al., 1986; Gordeev et al., 2015; Pedoja et al., 2006). On one side, the Pacific Plate subducts north-west beneath Kamchatka, forming the Kuril-Kamchatka trench, with a gradually decreasing angle from 55 degrees to 35 degrees (Gorbatov et al., 1997). On the other side, the Pacific slab subducts with an oblique angle northward along the Aleutian trench, where it turns into a transform boundary along the westernmost part of the trench. The Kuril-Kamchatka and Aleutian trenches intersect in the area of the Kamchatsky Cape, situated at approximately 56°N, at almost a right angle, forming an active junction where the subduction and transform boundary processes cause the collision of the westernmost segment of the Aleutian arc, referred to as the Komandorsky shear zone, with the Kamchatka Peninsula (Gordeev et al., 2015; Levina et al., 2013). North of the junction, no subduction occurs (Gaedicke et al., 2000), and the present trench is considered extinct (Alexeiev et al., 2006).

Due to the arc-continental collision, this area is fragmented into several fracture zones, which splay onshore on Kamchatsky Cape and are enclosed between the Alpha fracture zone in the north and the Naturalist fracture zone in the south. General dextral strike-slip faulting emerges due to the relative velocities between the rapidly moving Pacific Plate and the slow moving Komandorsky segment (Gaedicke et al., 2000).

The Kumroch Range, also called the Kumroch thrust belt, located directly west of Kamchatsky Cape, is the onshore response to the collision, as suggested by the folded rocks to the east and the fault systems that are right-lateral to the north and left-lateral to the south (Geist and Scholl, 1994). Some recent studies show that the Kumroch Range is actually part of a larger active fault system named the East Kamchatka Fault Zone (Kozhurin et al., 2006; Kozhurin and Zelenin, 2017). This fault zone stretches along the east coast over two-thirds of the peninsula and is composed of a hundred small predominantly normal NE-SW-oriented faults, which are connected to the late Quaternary volcanism of the region. The East Kamchatka Fault Zone is bounded on the west by the Central Kamchatka Depression, a wide valley that hosts some of the most active Kamchatka volcanoes: the Klyuchevskoy group of volcanoes, including Klyuchevskoy, Benzimiani and Tolbachik, and the Shiveluch volcano (Kozhurin et al., 2006). The main geological structure of the peninsula is composed of folded Cretaceous-Tertiary rocks, overlain by Quaternary units and overprinted by volcanic activity.

Earthquake-related faulting north of the subduction zone

It was believed that strong earthquakes and tsunamis are improbable north of the Pacific subduction zone. However, the November 22 1969 Mw 7.7 Ozernovskoe earthquake (Levina et al., 2013), the 24 June 2012 Mw 6.1 Near East Coast of Kamchatka earthquake and the latest 29

March 2017 Mw 6.6 Yuzhno-Ozernovskoe earthquake of reveal the active faulting structure and resulting seismogenic and tsunamigenic potential hazards of this region (see Fig. 1).

Most of the seismic activity is concentrated offshore in the fractured region frontal to the collision zone and along the Pacific-Aleutian transform boundary and normally achieves magnitudes of approximately 6. The last strong Mw. 7.2 earthquake along the transform region occurred close to Komandorskiye Island on December 20 2018. The onshore collision zone coincident with the Kumroch thrust belt is associated with low-level seismicity.

The 29 March 2017 Yuzhno-Ozernovskoe earthquake occurred immediately north of Kamchatsky Cape, where three different geological and tectonic structures interact with each other: the Pacific slab subduction edge, the East Kamchatka Fault Zone and the Komandorsky segment collision with the Kamchatka Peninsula. According to the Kamchatka Regional Seismic Network (see Data and Resources) the epicentre was located at 56.97°N and 162.22°E at a depth of approximately 43 km. Dozens of aftershocks have been recorded mainly in the first 3 months after the mainshock, some of them exceeding magnitude 5 (see Fig. 2).

[Figure 2]

Data and methods

Seismic Data

We exploit seismic records identified by the regional instrumental network. The Kamchatka Regional Seismic Network (KRSN) was initially set up in 1961. It currently includes 83 permanent seismic stations in the region (see Data and Resources). The KRSN is composed of three networks with different extents and resolution capabilities: a network of stationary digital seismic stations, a network of telemetered seismic stations (TSS), and a strong motion network

(SMN) (Chebrov et al., 2013; Gordeev et al., 2013). The KRSN is currently operated by the Kamchatka Branch of the Geophysical Survey of the Russian Academy of Sciences (KB GS RAS) and the seismic data are available through the Seismological Data Information System (SDIS) (see Data and Resources). The station distribution has a higher density in the northeastern part of the Central Kamchatka Depression and over the Kamchatka East Ridge, the two regions that host the most active volcanoes in Kamchatka, while only a few stations are located in the northern part of the peninsula where the Yuzhno-Ozernovskoe earthquake occurred (see Fig. 2). The hypocentre seismic source location is estimated using the arrival times of P- and S-waves. According to the local seismic catalogue, the epicentre was located 25 km offshore at a depth of 43 km with accuracies of 16 km in horizontal location and 20 km in depth (see Data and Resources).

As is well known, the source focal mechanism derived from seismic data provides two possible fault-plane solutions (nodal planes) that are located at right angles with respect to each other. The fault plane ambiguity can be solved only taking into consideration geological and additional geophysical data. The source focal mechanism as in (Chebrov et al., 2017) is retrieved by fixing the depth to 10 km and shows a NE-SW-oriented reverse fault with a small oblique component. The main shock was also detected by several global seismological centres: the Global Centroid Moment Tensor Project (GCMT) Catalogue; the United States Geological Survey (USGS); the GEOForschungsNetz (GEOFON); the National Institute of Geophysics and Volcanology (INGV); and the Global Network of Broadband Seismic Stations (GEOSCOPE) (see Data and Resources). All seismic derived results agree with the orientation of the fault and show dip angles ranging between 39° and 55° , although they disagree in the seismic source localization in

the range of dozens of km due to different seismic stations used for the inversion, different algorithms and consequently the type of source location, which is either hypocentre (focus), corresponding to the starting point of the rupture, or centroid, corresponding to the centre of energy released (see Fig. 3). The GCMT, USGS and GEOSCOPE provide the centroid solution of the earthquake, although they use different spectrums of the seismic waves; while the GCMT uses both long-period ($T > 45$ s) body waves and very-long-period ($T > 135$ s) surface waves (Dziewonski et al., 1981; Ekström et al., 2012), the USGS applies the so-called W-phase source inversion algorithm which uses long-period (100–1,000 s) phase arriving between the P- and S-wave phases (Hayes et al., 2009), and GEOSCOPE applies the SCARDEC method that uses teleseismic body waves (Vallée et al., 2011). GEOFON and INGV retrieve the seismic source hypocentre, the former by using the body wave amplitudes and polarities and the latter by applying the time-domain moment tensor technique using the broadband velocity waveforms. The GCMT solution locates the seismic centroid offshore close to Pokaty Canyon, similar to the local seismic epicentre solution, while GEOFON locates the earthquake epicentre onshore in the eastern part of the Kumroch thrust belt, close to the locations estimated by the USGS and GEOSCOPE centroid solutions. Considering all these different source solutions and their uncertainties, we conclude that based on only seismic source solutions, it is difficult to find a unique interpretation, especially in such a complex tectonic setting. Therefore, with the availability of co-seismic information from DInSAR, we can better understand the seismic source and therefore provide a much more accurate tectonic interpretation (Çakir et al., 2003; Fialko et al., 2005; Grandin et al., 2016; Lasserre et al., 2005; Sangha et al., 2017; Vajedian and Motagh, 2018).

[Figure 3]

DInSAR analysis

Two different SAR satellites are available for the co-seismic analysis: ALOS-2 L-band and Sentinel-1A C-band SAR sensors (see Data and Resources). From the ALOS-2 sensor, both ascending and descending orbit passes with temporal baselines of 350 days and 56 days, respectively, are suitable for interferometric analysis. For the Sentinel-1A mission the ascending orbit pass does not cover the area of interest well; therefore, only data from a descending pass is processed. The precise orbits have been used for all datasets. The main characteristics of the three SAR interferometric couples are summarized in Tab. 1.

[Table 1]

The DInSAR processing was performed using the commercial interferometric SARscape® 5.4.1 module in the Environment for Visualizing Images (ENVI) platform. The 30 m Shuttle Radar Topography Mission (SRTM) digital elevation model (Farr et al., 2007) was used to remove the topographic phase contribution and perform the transformation from radar to geographic coordinates. To enhance the signal-to-noise ratio (SNR) of the interferograms, a modified Goldstein filter was applied to the interferograms with filter window sizes of 32, 128 and 256 pixels for ALOS-2 ascending and descending and Sentinel-1A descending dataset, respectively (Baran et al., 2003; Ghulam et al., 2010; Goldstein and Werner, 1998). The phase-wrapped maps are shown in Fig. 4. The unwrapping step was performed by applying the minimum cost flow algorithm (Costantini, 1998; Reigber and Moreira, 1997) and selecting coherence thresholds of 0.15 for the ALOS-2 ascending and Sentinel-1A descending datasets and 0.1 for the ALOS-2 descending dataset. The low coherence values are mostly due to snow cover, and for the ALOS-2

datasets, they are also a result of temporal decorrelation related to the longer time span between the scenes. Finally, the unwrapped phase was transformed into a displacement value with respect to a selected reference point considered to be stable and geocoded to projected coordinate system WGS84/UTM zone 58N (see Figs. 4 and 5).

[Figure 4]

From the interferometric analysis, three co-seismic displacement maps were produced, each showing the 1D radar line-of-sight (LOS) displacement component, which corresponds to the direction between the ground target and the radar sensor. The deformation pattern of the concentric to the coast displacement field clearly shows that the seismic source was located offshore. Motions of the ground towards the sensors were detected from both acquisition geometries, corresponding to uplift and westward movements. The maximum LOS displacement in the ascending orbit was 19 cm, while in the two descending orbit acquisitions, it is approximately 15 cm for Sentinel-1A and 19 cm for ALOS-2 (see Fig. 5). The observations from three different projections of the displacement vector allowed us to perform a 2D decomposition in the vertical and east-west directions, which show a maximum uplift of approximately 20 cm and a horizontal westward motion of approximately 7 cm (see Supplemental Material). The two ALOS-2 acquisitions, which include several months after the earthquake, are affected by post-seismic deformation (see Fig. 2). An additional descending ALOS-2 interferogram was processed using radar scenes acquired on 27/06/2016 and 26/06/2017 to evaluate possible aftershock contributions. The residuals between the two ALOS-2 descending displacement maps show that the post-seismic displacement is irrelevant, and thus, the aftershock contribution may be neglected (see Supplemental Material).

Geodetic Modelling and Results

The three DInSAR datasets were jointly inverted using a two-step inversion procedure: first, a non-linear inversion to define the source geometry and rupture mechanism and second, a linear inversion to retrieve the slip distribution on the previously modelled fault plane. Both inversion steps were carried out using the least squares approach. The overall modelling was conducted with the SARscape® modelling module. As a preliminary stage, the datasets were subsampled in a regular grid using two different sampling densities of 150 m and 500 m over the area affected by the maximum displacement and the surroundings and generating a set of approximately 3000 points. The first inversion step is a non-linear inversion of the DInSAR displacement measurements assuming single rectangular uniform dislocation in a homogeneous and elastic half-space (Okada, 1985). The Levenberg-Marquardt least squares algorithm (Marquardt, 1963) was applied to solve the optimization problem and implemented with multiple restarts to guarantee that the global minimum of the least squares misfit between the model and observations is reached. The following cost function (CF) is minimized:

$$CF = \sum_{i=1}^n W_d \frac{1}{N} \sum_{i=1}^N \frac{(d_{iobs} - d_{imod})^2}{\sigma_i}$$

where n is the number of datasets, W_d is the dataset weighting coefficient, N is the number of sampling points, $d_{i\text{ obs}}$ and $d_{i\text{ mod}}$ are the observed and modelled displacement of the i -th point and σ_i is the standard deviation for all points (Atzori et al., 2009). We adopted the same weighting coefficient of 1 for all three datasets.

The focal mechanism derived from seismological data was used to define the initial parameter intervals, while length and width intervals were chosen in agreement with the empirical magnitude-area scale laws (Wells and Coppersmith, 1994).

Based on structural geology and geophysical data (Gaedicke et al., 2000; Geist and Scholl, 1994; Kozhurin et al., 2006), we assumed a west-dipping fault plane for the inversion. A global minimum of the square misfit, and therefore a best fit between the model-predicted deformations and the three DInSAR datasets, is easily reached under the hypothesis of N-NW reverse or oblique dipping. To facilitate the inversion process, we fixed the maximum slip to 2.5 m, in agreement with the empirical magnitude-slip scale laws (Wells and Coppersmith, 1994). Under the aforementioned conditions, the geodetic moment of the best-fit solution is consistent with the seismic moment $8.75\text{E}+8$ Nm, equivalent to a magnitude 6.59 Mw. The overall root mean square (RMS) misfits between the DInSAR data and the model-predicted deformation for a uniform slip patch are approximately 12, 6 and 3 mm for ALOS-2 ascending and descending and Sentinel-1A descending datasets, respectively.

In contrast to seismic solutions from the local and global seismological centres, which indicate the location of the earthquake being onshore or approximately 20 km offshore close to Pokaty Canyon, the location of the centre of the fault retrieved from the first inversion step is approximately 5 km offshore. To check the location of the source, we constrained the coordinate intervals first closer to Pokaty Canyon, as suggested by the GCMT centroid solution and the local seismic epicentre solution. Under the aforementioned conditions, the model cannot fit the observed displacement fields well, and the RMS increases to approximately 24, 19 and 17 mm for ALOS-2 ascending and descending and Sentinel-1A descending datasets, respectively. Moreover the geodetic moment is much higher than the seismic moment ($1.66\text{E}+9$ Nm, equivalent to a magnitude 6.78 Mw). We performed a second inversion by constraining the centroid location inland as suggested by the rest of the seismological centers. This also led to

higher geodetic moment as compared to the seismic moment ($1.41\text{E}+9$ Nm, equivalent to a magnitude 6.73 Mw), although the model-observations misfit is lower (the RMS are approximately 12, 7 and 5 mm for ALOS-2 ascending and descending and Sentinel-1A descending datasets, respectively). Moreover, the estimated geometric parameters are not consistent with the empirical magnitude-area scale laws, as the estimated width of the fault plane is much larger than the respective estimated length. For the aforementioned reason, we excluded that the centroid's location is further offshore or inland. Finally, we also performed the modelling by assuming an east-dipping fault plane. Under this condition, we obtained a SE dipping thrust fault characterized by approximately 22° dip angle, and located approximately 5 km offshore, similar in location as in the west-dipping assumption. The model fits the observations quite well (the RMS are approximately 12, 6 and 4 mm for ALOS-2 ascending and descending and Sentinel-1A descending datasets, respectively). However the geodetic moment for the east-dipping fault is lower than the seismic moment ($7.57\text{E}+8$ Nm, equivalent to a magnitude 6.55 Mw). Therefore, based on this final outcome and on the structural geology we excluded the hypothesis of east-dipping fault.

The final fault model parameters are reported in Fig. 4. The best-fit model suggests a shallow north-west-dipping reverse rupture with a right-lateral component. The three model-predicted deformations and respective residuals are shown in Fig. 5. The residual signal is almost absent in the two descending geometries and indicates that no secondary fault structures were activated following the mainshock. The residual signal in the ascending geometry is higher and most likely related to temporal decorrelation errors due to the one-year temporal baseline.

[Table 2]

[Figure 5]

To estimate the source parameter uncertainties and the parameter trade-off related to the propagation effect of noise in the DInSAR data, we solved the non-linear inversion optimization for 120 independent samplings by adding to the initial datasets a certain correlated noise, which was estimated based on the interferometric data covariance in an area of the interferogram where displacement is expected to be null (Cervelli et al., 2001; Sudhaus and Sigurjón, 2009). Source model parameters, covariances and uncertainty intervals reporting the parameters best-fit, mean and standard deviation values are shown in Fig. 6 a) and in Tab. 2. Compared to studies in which the deformation field of a fault is completely covered by DInSAR (Motagh et al., 2015; Pedersen et al., 2003) the standard deviation values that we derived for geometrical parameters, e.g., length and width, are relatively large. This results is not surprising because the displacement field detected by geodetic measurements in offshore fault systems covers only the coastal area, and we have no information on what occurred under water (Biggs et al., 2009; Hooper et al., 2013; Motagh et al., 2008). However, the source location is quite well constrained, and the standard deviations of the East and North coordinates are approximately 1 km. The obvious trade-off between the dislocation area and slip is not visible as the maximum slip value was fixed in agreement with the empirical magnitude-slip scale laws in order to facilitate the non-linear optimization. A significant trade-off is visible between the spatial coordinates and the dislocation geometry orientation (strike, dip and rake) and between the plane dip angle and the source depth.

[Figure 6]

Once the fault geometry was modeled for a uniform slip, we divided the fault plane into 1 km² quadratic patches. We solved the linear inversion with respect to the slip using the non negative

least squares algorithm (Lawson and Hanson, 1995) and considering a fixed rake direction of 109°. We extended the fault plane length to 30 km and width to 20 km to eliminate border effects. A smoothing Laplacian operator (∇^2) was applied, weighted by an empirical coefficient k of 0.001, in order to correlate the slip values of the neighbouring sub-areas. The slip distribution was obtained for each patch by linearly inverting the system:

$$\begin{bmatrix} Alos_{asc} \\ Alos_{desc} \\ S1_{desc} \end{bmatrix} = \begin{bmatrix} G \\ k\nabla^2 \end{bmatrix} \cdot s$$

where G is Green's matrix and s is the slip model vector (Harris and Segall, 1987; Motagh et al., 2006; Wright et al., 2003).

The main dislocation region corresponds to an area of approximately 11x10 km, at a depth interval between 6 and 14 km (see Fig. 6 b) and d)). The maximum slip is approximately 2.7 m at a depth of 10 km. The geodetic moment released from the distributed slip is 9E+18 Nm, equivalent to Mw. 6.6. The overall root mean square (RMS) misfits between the DInSAR data and the model-predicted deformation in the linear inversion are, as in the non-linear inversion, approximately 12, 6 and 3mm for ALOS-2 ascending and descending and Sentinel-1A descending datasets, respectively.

In the case of linear inversion, it is much more difficult to compute and visually represent the slip distribution uncertainty because it must be computed for a large number of parameters equivalent to the number of patches and taking into account the propagation effect of the noise in the InSAR data and the uncertainty of the geometric fault parameters previously modelled. In this study, we obtained uncertainty related only to the data noise propagation by considering a fixed source geometry. The complete uncertainty covariance matrix is calculated as (Atzori et al., 2008):

$$[cov_m] = G^{-g}[cov_d]G^{-gT}$$

where G^g is the generalized inverse matrix, cov_d is the interferometric data covariance and cov_m is the $N \times N$ symmetric parameter covariance matrix, where N is the number of patches with diagonal equivalent to the slip variance for each patch, while off-diagonal values correspond to the covariance between two different patches. Fig. 6 c) shows the slip distribution standard deviation for each patch, which is on the order of 1-3 cm. It is important to highlight that this is only the variance-diagonal of the covariance matrix, and therefore, it does not account for the slip correlations between different patches.

Discussion

A correct geodynamic interpretation in complex tectonic settings where several structures interact with each other can be achieved only if the active fault location can be constrained as accurately as possible. The use of both seismic and geodetic data helps to improve the location accuracy (Elliott et al., 2010; Fielding et al., 2013; Li et al., 2011; Xu et al., 2010), although the presence of seismic stations and ground geodetic instruments is scattered in many remote and difficult-to-access regions. In this regard, the DInSAR satellite geodetic technique is a valuable tool for geodetic data measurement over large areas and for geodetic modelling of the seismic source (Biggs et al., 2006; Nissen et al., 2019; Wright et al., 2003).

In our case study, the regional seismic stations have an inhomogeneous distribution and a poor coverage in the northern part of the peninsula exactly where the Yuzhno-Ozernovskoe earthquake occurred. Moreover, the available ground geodetic instruments are sparse and far from the area of displacement; therefore, DInSAR measurements are the only geodetic available data covering the region of interest. Due to the snow cover, temporal decorrelations, and low signal-to-noise ratio, it was essential to apply interferometric phase filtering during the

interferometric processing to enhance the signal and improve the readability of the deformation field.

With regard to the geodetic modelling, an essential aspect to take into account is the dependency of the source model on the initial source parameter intervals and constraints. The optimization algorithm may lead to completely different global minimum values and thus also to geophysically unrealistic source models. Moreover, the ambiguity of the seismic based focal mechanism solution, leads to the definition of two equally probable nodal planes. It is fundamental at this initial step to use all geological and geodynamic knowledge and the empirical parameter scale-laws to set up the most appropriate initial conditions. In our study, we used the seismic solutions to define the initial intervals for the non-linear inversion. The fault model that best fits the three displacement observations and that is characterized by a geodetic moment compatible with the seismic one has the following initial conditions: 1. N-NW dip; 2. reverse or oblique movement; and 3. maximum uniform slip of 2.5 m. The fault model parameter uncertainties and parameter trade-off were estimated by considering the propagation effects of noise in the DInSAR data. The results show that the source location (East, North and depth) is quite well constrained with an accuracy of approximately 1 km, while what seems less constrained is the fault size, as the derived accuracy of the length and width is approximately 2.4 km. However, considering that length and width are approximately 10 km, an accuracy of 2.4 km is well acceptable. The slip distribution variance was also estimated, however the method used takes only into account the propagation effect of noise in the InSAR data, without considering the propagation effects of the fault model parameter uncertainties and the correlations between the different patches. The slip distribution variance obtained is of the order of 2-3 cm.

Our final fault model is consistent with the type and orientation of the source derived from seismic data, although there are two main discrepancies related to the fault location and dip angle. From local seismic data, the epicentre was located approximately 20 km offshore, close to the GCMT centroid location. These two solutions could suggest that the rupture occurred on a fault coincident with Pokaty Canyon or part of the extinct trench. However, based on the DInSAR co-seismic measurements, we obtained that in order to generate such onshore deformations, a much higher magnitude earthquake is required. The other seismic solutions locate the epicentre onshore on the Kumroch Ridge. However, under this constraint, we obtained an unrealistic fault plane geometry. The concentric fringe pattern of co-seismic deformation on the coast, in fact, is an explicit indicator that the fault plane is most likely to be located offshore (Motagh et al., 2008). We also tested the hypothesis of an east-dipping fault plane. Under this condition the geodetic moment obtained for the best-fit source model is lower than the seismic moment, indicating that for the east-dipping plane a lower magnitude earthquake would have been responsible for the measured co-seismic deformations.

Our detailed reconstruction of the regional fault system based on currently available studies (Hindle et al., 2019; Ponomareva et al., 2007; Timofeev et al., 2012) and Russian geological data (see Data and Resources) allowed us to interpret the retrieved new fault as part of an offshore prolongation of the Kumroch Ridge, which in recent studies (Kozhurin et al., 2006; Kozhurin and Zelenin, 2017) is considered part of a larger fault system named the East Kamchatka Fault Zone. The steep dip angle indicates that the rupture did not occur at the edge of the Pacific subduction slab, which dips at an angle of approximately 35° . The north-west-dipping fault and the reverse mechanism with consequent uplift and westward horizontal deformation components

detected on the coast are consistent with the Komandorsky segment collision with the Kamchatka Peninsula occurring immediately south of this region, which produces a westward compressional stress with reverse faulting visible in the Kumroch thrust belt (see Figs. 2 and 7 and also Supplemental Material). By integrating our results with the already known fault systems of Kamchatka, we suggest that the East Kamchatka Fault Zone extends farther north to the Okhotsk microplate boundary with the North American Plate both onshore and offshore. Due to the arc-continental collision at the latitude of Kamchatsky Cape, its predominant mid-late Quaternary normal faults turn into the thrust fault system coincident with the Kumroch Range. The South-Ozernovskoe earthquake fault model proves that the Kumroch thrust belt is an active fault zone driven by the arc-continental strain mechanism and extends even offshore.

[Figure 7]

Conclusions

In this study, we investigate the potential of differential SAR interferometry for understanding complex tectonic settings where ground geodetic observations are absent and seismic stations are not well distributed. The co-seismic displacement produced by the 29 March 2017 Mw 6.6 South-Ozernovskoe Kamchatka earthquake is successfully detected from multi-sensor/multi-orbit DInSAR measurements. Three independent SAR datasets, ALOS-2 ascending and descending and Sentinel-1A descending, are processed and jointly inverted using an elastic half-space fault model.

An uplift of approximately 20 cm and a westward displacement component of approximately 7 cm were induced by the earthquake on the coast north of Kamchatsky Cape. The final fault model suggests a crustal reverse fault with a right-lateral component, located approximately 5

km offshore, dipping north-west at an angle of 72° and producing a maximum slip of 2.7 m at a depth of approximately 10 km. The seismic moment released from the distributed slip is estimated to have been $9\text{E}+18$ Nm, equivalent to Mw 6.6. The fault model suggests that the rupture occurred on a fault system that is the offshore extension of the Kumroch thrust belt. This earthquake provides evidence for neotectonic activity related to the arc-continental collision process. Moreover, the Kumroch thrust belt can be considered part of the East Kamchatka Fault Zone, a larger active fault system stretching over two-thirds of the Kamchatka Peninsula. Additionally, our fault model confirms that the fault system extends farther north, likely to the Okhotsk microplate boundary with the North American Plate. The outcomes of this research demonstrate that the area north of the Pacific slab subduction zone, which had long been considered aseismic, is characterized by higher seismic and tsunamigenic hazards than previously thought. In general, we provide evidence for the great potential of using InSAR techniques for better insight into complex tectonic settings, especially in remote and difficult-to-access regions.

Data and Resources

Sentinel- 1 Synthetic Aperture Radar (SAR) images were provided by the European Space Agency (ESA) and freely downloadable from <https://scihub.copernicus.eu> (last accessed in June, 2019). Sentinel-1 Precise Orbit Ephemerides have been downloaded from https://qc.sentinel1.eo.esa.int/aux_poeorb/ (last accessed in June, 2019) Original ALOS-2 data is copyright of Japanese Aerospace agency and were provided under proposal 1162.

437 Shuttle Radar Topography Mission (SRTM) V1 is the digital elevation model data avoid filled at
438 a resolution of 1 arc-second (30 meters) downloaded from EarthExplorer USGS portal
439 (<https://earthexplorer.usgs.gov/>) (Digital Object Identifier (DOI) number: /10.5066/F7PR7TFT).
440 DInSAR and fault modelling processes have been performed using SARscape ©ENVI software
441 modul.

442 The Global Centroid Moment Tensor Project (GCMT) database was searched using
443 <https://www.globalcmt.org/CMTsearch.html> (last accessed in June, 2019). United States
444 Geological Survey (USGS) database was searched using
445 <https://earthquake.usgs.gov/earthquakes/browse/> (last accessed in June, 2019). The
446 GEOForschungsNetz (GEOFON) database was searched using [https://geofon.gfz-](https://geofon.gfz-potsdam.de/eqinfo/form.php)
447 [potsdam.de/eqinfo/form.php](https://geofon.gfz-potsdam.de/eqinfo/form.php) (last accessed in June, 2019). The Global Network of Broadband
448 Seismic Stations (GEOSCOPE) was searched using <http://geoscope.ipgp.fr/index.php/en/> (last
449 accessed in June, 2019). The National Institute of Geophysics and Volcanology (INGV) was
450 searched using <http://cnt.rm.ingv.it/> (last accessed in June, 2019). The Seismological Data
451 Information System of Kamchatka Branch of Geophysical Survey of Russian Academy of
452 Science Earthquakes Catalogue for Kamchatka and the Commander Islands (1962–present)
453 (SDIS - KB GS RAS) database was searched using
454 <http://sdis.emsd.ru/info/earthquakes/catalogue.php> (last accessed in June, 2019). Kamchatka
455 Branch of Geophysical Survey of Russian Academy of Science, Information on seismic stations
456 <http://sdis.emsd.ru/info/instruments/seismostations.php> (last accessed in March, 2020)

Digital GIS-Model Kamchatka (from GIS-Atlas NEDRA ROSSII 2018), Ministry of Natural Resources and Ecology of the Russian Federation, Federal Agency of Mineral Resources, Russian Geological Research Institute <http://atlaspacket.vsegei.ru> (last accessed in June, 2019). Natural Earth image freely downloadable <https://www.naturalearthdata.com/> (last accessed in June, 2019).

This electronic supplement contains three additional figures. Figure S1 shows detailed reconstruction of the tectonic setting, faulting system and main geological units of Kamchatka region, and should be consulted together with Figure 1. Figure S2 shows the 2D displacement decomposition and after-shock residuals, and it is supplementary information to Figure 5. Figure S3 shows a detailed view of Figure S1 over a restricted to the the 29 March 2017 Yuzhno-Ozernovskoe Kamchatka earthquake region, with added the seismic data and the fault model horizontal projection, which help to contextualize the event and provide the geodynamic interpretation. This final figure is supplementary to Figure 7.

Acknowledgments

We thank the Japanese and European space agencies for ALOS-2 and Sentinel-1 satellite radar data, respectively, and all the seismological agencies (Global Centroid Moment Tensor Project, United States Geological Survey, GEOForschungsNetz, National Institute of Geophysics and Volcanology, Global Network of Broadband Seismic Stations and Seismological Data Information System of Kamchatka Branch of Geophysical Survey of Russian Academy of Science Earthquakes Catalogue for Kamchatka and the Commander Islands (1962–present)) for the earthquake mechanism parameter values used to set up the initial model parameter intervals. We thank the Geological Research Institute of the Ministry of Natural Resources and Ecology of

the Russian Federation (Federal Agency of Mineral Resources, Russian) for the geological data. We thank Harris Geospatial Solutions, Inc and sarmap for developing and providing SARscape® 5.4.1 module in the Environment for Visualizing Images (ENVI) platform used to perform the main processing steps. We thank QGIS project for providing the geographic information system tool used in this work.

Reference

- Alexeiev, D.V., Gaedicke, C., Tsukanov, N.V., Freitag, R., 2006. Collision of the Kronotskiy arc at the NE Eurasia margin and structural evolution of the Kamchatka–Aleutian junction. *Int. J. Earth Sci.* 95, 977–993. <https://doi.org/10.1007/s00531-006-0080-z>
- Apperson, K.D., 1991. Stress Fields of the Overriding Plate at Convergent Margins and Beneath Active Volcanic Arcs. *Science* 254, 670–678. <https://doi.org/10.1126/science.254.5032.670>
- Atzori, S., Hunstad, I., Chini, M., Salvi, S., Tolomei, C., Bignami, C., Stramondo, S., Trasatti, E., Antonioli, A., Boschi, E., 2009. Finite fault inversion of DInSAR coseismic displacement of the 2009 L’Aquila earthquake (central Italy). *Geophys. Res. Lett.* 36. <https://doi.org/10.1029/2009GL039293>
- Baer, G., Funning, G.J., Shamir, G., Wright, T.J., 2008. The 1995 November 22, Mw 7.2 Gulf of Elat earthquake cycle revisited. *Geophys. J. Int.* 175, 1040–1054. <https://doi.org/10.1111/j.1365-246X.2008.03901.x>
- Bagnardi, M., Hooper, A., 2018. Inversion of Surface Deformation Data for Rapid Estimates of Source Parameters and Uncertainties: A Bayesian Approach. *Geochem. Geophys. Geosystems* 19, 2194–2211. <https://doi.org/10.1029/2018GC007585>

501 Baran, I., Stewart, M.P., Kampes, B.M., Perski, Z., Lilly, P., 2003. A modification to the
 502 Goldstein radar interferogram filter. *IEEE Trans. Geosci. Remote Sens.* 41, 2114–2118.
 503 <https://doi.org/10.1109/TGRS.2003.817212>

504 Biggs, J., Bergman, E., Emmerson, B., Funning, G.J., Jackson, J., Parsons, B., Wright, T.J.,
 505 2006. Fault identification for buried strike-slip earthquakes using InSAR: The 1994 and
 506 2004 Al Hoceima, Morocco earthquakes. *Geophys. J. Int.* 166, 1347–1362.
 507 <https://doi.org/10.1111/j.1365-246X.2006.03071.x>

508 Bürgmann, R., Kogan, M.G., Steblov, G.M., Hilley, G., Levin, V.E., Apel, E., 2005. Interseismic
 509 coupling and asperity distribution along the Kamchatka subduction zone. *J. Geophys.*
 510 *Res. Solid Earth* 110. <https://doi.org/10.1029/2005JB003648>

511 Çakir, Z., Chabalier, J.-B. de, Armijo, R., Meyer, B., Barka, A., Peltzer, G., 2003. Coseismic and
 512 early post-seismic slip associated with the 1999 Izmit earthquake (Turkey), from SAR
 513 interferometry and tectonic field observations. *Geophys. J. Int.* 155, 93–110.
 514 <https://doi.org/10.1046/j.1365-246X.2003.02001.x>

515 Cervelli, P., Murray, M.H., Segall, P., Aoki, Y., Kato, T., 2001. Estimating source parameters
 516 from deformation data, with an application to the March 1997 earthquake swarm off the
 517 Izu Peninsula, Japan. *J. Geophys. Res. Solid Earth* 106, 11217–11237.
 518 <https://doi.org/10.1029/2000JB900399>

519 Chebrov, D.V., Kugaenko, Yu.A., Lander, A.V., Abubakirov, I.R., Voropaev, P.V., Gusev, A.A.,
 520 Droznin, D.V., Droznina, S.Ya., Ivanova, E.I., Kravchenko, N.M., Matveenko, E.A.,
 521 Mitushkina, S.V., Ototuk, D.A., Pavlov, V.M., Rayevskaya, A.A., Saltikov, V.A.,
 522 Senyukov, S.L., Skorkina, A.A., Serafimova, Yu.K., 2017. ЮЖХО-ОЗЕПНОБСКОЕ

523 ЗЕМЛЕТРЯСЕНИЕ 29.03.2017 г. с $MW = 6.6$, $KS = 15.0$, $I = 6$ (КАМЧАТКА).. The
 524 Match 29th, 2017 earthquake with $KS = 15.0$, $MW = 6.6$, $I = 6$ in the Ozernoy Gulf
 525 (Kamchatka) Vestnik KRAUNC, 7–21.
 526 Chebrov, V.N., Droznin, D.V., Kugaenko, Yu.A., Levina, V.I., Senyukov, S.L., Sergeev, V.A.,
 527 Shevchenko, Yu.V., Yashchuk, V.V., 2013. The system of detailed seismological
 528 observations in Kamchatka in 2011. J. Volcanol. Seismol. 7, 16–36.
 529 <https://doi.org/10.1134/S0742046313010028>
 530 Cook, D.B., Fujita, K., McMullen, C.A., 1986. Present-day plate interactions in Northeast Asia:
 531 North American, Eurasian, and Okhotsk plates. J. Geodyn., Proceedings of the
 532 Symposium Polar Geophysics 6, 33–51. [https://doi.org/10.1016/0264-3707\(86\)90031-1](https://doi.org/10.1016/0264-3707(86)90031-1)
 533 Costantini, M., 1998. A novel phase unwrapping method based on network programming. IEEE
 534 Trans. Geosci. Remote Sens. 36, 813–821. <https://doi.org/10.1109/36.673674>
 535 DeMets, C., Gordon, R.G., Argus, D.F., Stein, S., 1990. Current plate motions. Geophys. J. Int.
 536 101, 425–478. <https://doi.org/10.1111/j.1365-246X.1990.tb06579.x>
 537 Diao, F., Walter, T.R., Motagh, M., Prats-Iraola, P., Wang, R., Samsonov, S.V., 2015. The 2015
 538 Gorkha earthquake investigated from radar satellites: slip and stress modeling along the
 539 MHT. Front. Earth Sci. 3. <https://doi.org/10.3389/feart.2015.00065>
 540 Elliott, J.R., Walters, R.J., England, P.C., Jackson, J.A., Li, Z., Parsons, B., 2010. Extension on
 541 the Tibetan plateau: recent normal faulting measured by InSAR and body wave
 542 seismology: Extension on the Tibetan plateau. Geophys. J. Int. 183, 503–535.
 543 <https://doi.org/10.1111/j.1365-246X.2010.04754.x>
 544 Fialko, Y., Sandwell, D., Simons, M., Rosen, P., 2005. Three-dimensional deformation caused

by the Bam, Iran, earthquake and the origin of shallow slip deficit. *Nature* 435, 295.
<https://doi.org/10.1038/nature03425>

Fielding, E.J., Sladen, A., Li, Z., Avouac, J.-P., Bürgmann, R., Ryder, I., 2013. Kinematic fault slip evolution source models of the 2008 M7.9 Wenchuan earthquake in China from SAR interferometry, GPS and teleseismic analysis and implications for Longmen Shan tectonics. *Geophys. J. Int.* 194, 1138–1166. <https://doi.org/10.1093/gji/ggt155>

Freitag, R., Gaedicke, C., Baranov, B., Tsukanov, N., 2001. Collisional processes at the junction of the Aleutian–Kamchatka arcs: new evidence from fission track analysis and field observations. *Terra Nova* 13, 433–442. <https://doi.org/10.1046/j.1365-3121.2001.00375.x>

Gaedicke, C., Baranov, B., Seliverstov, N., Alexeiev, D., Tsukanov, N., Freitag, R., 2000. Structure of an active arc-continent collision area: the Aleutian–Kamchatka junction. *Tectonophysics* 325, 63–85. [https://doi.org/10.1016/S0040-1951\(00\)00131-1](https://doi.org/10.1016/S0040-1951(00)00131-1)

Geist, E.L., Scholl, D.W., 1994. Large-scale deformation related to the collision of the Aleutian Arc with Kamchatka. *Tectonics* 13, 538–560. <https://doi.org/10.1029/94TC00428>

Ghulam, A., Amer, R., Ripperdan, R., 2010. A filtering approach to improve deformation accuracy using large baseline, low coherence DInSAR phase images, in: 2010 IEEE International Geoscience and Remote Sensing Symposium. Presented at the 2010 IEEE International Geoscience and Remote Sensing Symposium, pp. 3494–3497. <https://doi.org/10.1109/IGARSS.2010.5652581>

Goldstein, R.M., Werner, C.L., 1998. Radar interferogram filtering for geophysical applications. *Geophys. Res. Lett.* 25, 4035–4038. <https://doi.org/10.1029/1998GL900033> @ 10.1002/(ISSN)1944-8007.GRL40

567 Gorbatov, A., Kostoglodov, V., Suárez, G., Gordeev, E., 1997. Seismicity and structure of the
 568 Kamchatka Subduction Zone. *J. Geophys. Res. Solid Earth* 102, 17883–17898.
 569 <https://doi.org/10.1029/96JB03491>

570 Gordeev, E.I., Fedotov, S.A., Chebrov, V.N., 2013. Detailed seismological investigations in
 571 Kamchatka during the 1961–2011 period: Main results. *J. Volcanol. Seismol.* 7, 1–15.
 572 <https://doi.org/10.1134/S0742046313010041>

573 Gordeev, E.I., Pinegina, T.K., Lander, A.V., Kozhurin, A.I., 2015. Beringia: Seismic hazard and
 574 fundamental problems of geotectonics. *Izv. Phys. Solid Earth* 51, 512–521.
 575 <https://doi.org/10.1134/S1069351315030039>

576 Grandin, R., Klein, E., Métois, M., Vigny, C., 2016. Three- dimensional displacement field of
 577 the 2015 Mw8.3 Illapel earthquake (Chile) from across- and along- track Sentinel- 1
 578 TOPS interferometry. *Geophys. Res. Lett.* 43, 2552–2561.
 579 <https://doi.org/10.1002/2016GL067954>

580 Hindle, D., Sedov, B., Lindauer, S., Mackey, K., 2019. The Ulakhan fault surface rupture and the
 581 seismicity of the Okhotsk–North America plate boundary. *Solid Earth* 10, 561–580.
 582 <https://doi.org/10.5194/se-10-561-2019>

583 Johnson, J.M., Satake, K., 1999. Asperity Distribution of the 1952 Great Kamchatka Earthquake
 584 and its Relation to Future Earthquake Potential in Kamchatka, in: Sauber, J., Dmowska,
 585 R. (Eds.), *Seismogenic and Tsunamigenic Processes in Shallow Subduction Zones*.
 586 Birkhäuser Basel, Basel, pp. 541–553. https://doi.org/10.1007/978-3-0348-8679-6_8

587 Kozhurin, A., Acocella, V., Kyle, P.R., Lagmay, F.M., Melekestsev, I.V., Ponomareva, V., Rust,
 588 D., Tibaldi, A., Tunesi, A., Corazzato, C., Rovida, A., Sakharov, A., Tengonciang, A.,

589 Uy, H., 2006. Trenching studies of active faults in Kamchatka, eastern Russia:
 590 Palaeoseismic, tectonic and hazard implications. *Tectonophysics* 417, 285–304.
 591 <https://doi.org/10.1016/j.tecto.2006.01.004>

592 Kozhurin, A., Zelenin, E., 2017. An extending island arc: The case of Kamchatka.
 593 *Tectonophysics* 706–707, 91–102. <https://doi.org/10.1016/j.tecto.2017.04.001>

594 Lasserre, C., Peltzer, G., Crampé, F., Klinger, Y., Van der Woerd, J., Tapponnier, P., 2005.
 595 Coseismic deformation of the 2001 M-w=7.8 Kokoxili earthquake in Tibet, measured by
 596 synthetic aperture radar interferometry. *J. Geophys. Res.-Solid Earth* 110.

597 Levina, V.I., Lander, A.V., Mityushkina, S.V., Chebrova, A.Yu., 2013. The seismicity of the
 598 Kamchatka region: 1962–2011. *J. Volcanol. Seismol.* 7, 37–57.
 599 <https://doi.org/10.1134/S0742046313010053>

600 Li, Z., Elliott, J.R., Feng, W., Jackson, J.A., Parsons, B.E., Walters, R.J., 2011. The 2010 M W
 601 6.8 Yushu (Qinghai, China) earthquake: Constraints provided by InSAR and body wave
 602 seismology. *J. Geophys. Res.* 116. <https://doi.org/10.1029/2011JB008358>

603 Marquardt, D., 1963. An Algorithm for Least-Squares Estimation of Nonlinear Parameters. *J.*
 604 *Soc. Ind. Appl. Math.* 11, 431–441. <https://doi.org/10.1137/0111030>

605 Motagh, M., Hoffmann, J., Kampes, B., Baes, M., Zschau, J., 2007. Strain accumulation across
 606 the Gazikoy–Saros segment of the North Anatolian Fault inferred from Persistent
 607 Scatterer Interferometry and GPS measurements. *Earth Planet. Sci. Lett.* 255, 432–444.
 608 <https://doi.org/10.1016/j.epsl.2007.01.003>

609 Motagh, M., Schurr, B., Anderssohn, J., Cailleau, B., Walter, T.R., Wang, R., Villotte, J.-P.,
 610 2010. Subduction earthquake deformation associated with 14 November 2007, Mw 7.8

611 Tocopilla earthquake in Chile: Results from InSAR and aftershocks. *Tectonophysics* 490,
612 60–68. <https://doi.org/10.1016/j.tecto.2010.04.033>

613 Müller, R.D., Dyksterhuis, S., Rey, P., 2012. Australian paleo-stress fields and tectonic
614 reactivation over the past 100 Ma. *Aust. J. Earth Sci.* 59, 13–28.
615 <https://doi.org/10.1080/08120099.2011.605801>

616 Nissen, E., Ghods, A., Karasözen, E., Elliott, J.R., Barnhart, W.D., Bergman, E.A., Hayes, G.P.,
617 Jamal- Reyhani, M., Nemati, M., Tan, F., Abdulnaby, W., Benz, H.M., Shahvar, M.P.,
618 Talebian, M., Chen, L., 2019. The 12 November 2017 Mw 7.3 Ezgeleh- Sarpolzahab
619 (Iran) Earthquake and Active Tectonics of the Lurestan Arc. *J. Geophys. Res. Solid Earth*
620 124, 2124–2152.

621 Okada, Y., 1985. Surface deformation due to shear and tensile faults in a half-space. *Bull.*
622 *Seismol. Soc. Am.* 75, 1135–1154.

623 Pedoja, K., Bourgeois, J., Pinegina, T., Higman, B., 2006. Does Kamchatka belong to North
624 America? An extruding Okhotsk block suggested by coastal neotectonics of the Ozernoi
625 Peninsula, Kamchatka, Russia. *Geology* 34, 353–356. <https://doi.org/10.1130/G22062.1>

626 Ponomareva, V., Melekestsev, I., Braitseva, O., Churikova, T., Pevzner, M., Sulerzhitsky, L.,
627 2007. Late Pleistocene-Holocene volcanism on the Kamchatka Peninsula, Northwest
628 Pacific Region, in: Eichelberger, J., Gordeev, E., Izbekov, P., Kasahara, M., Lees, J.
629 (Eds.), *Geophysical Monograph Series*. American Geophysical Union, Washington, D.
630 C., pp. 165–198. <https://doi.org/10.1029/172GM15>

631 Reigber, A., Moreira, J., 1997. Phase unwrapping by fusion of local and global methods, in:
632 *IGARSS'97. 1997 IEEE International Geoscience and Remote Sensing Symposium*

Proceedings. Remote Sensing - A Scientific Vision for Sustainable Development.
 Presented at the IGARSS'97. 1997 IEEE International Geoscience and Remote Sensing
 Symposium Proceedings. Remote Sensing - A Scientific Vision for Sustainable
 Development, pp. 869–871 vol.2. <https://doi.org/10.1109/IGARSS.1997.615282>
 Sangha, S., Peltzer, G., Zhang, A., Meng, L., Liang, C., Lundgren, P., Fielding, E., 2017. Fault
 geometry of 2015, Mw7.2 Murghab, Tajikistan earthquake controls rupture propagation:
 Insights from InSAR and seismological data. *Earth Planet. Sci. Lett.* 462, 132–141.
<https://doi.org/10.1016/j.epsl.2017.01.018>
 Scott, C.P., Arrowsmith, R., Nissen, E., Lajoie, L., Maruyama, T., Chiba, T., 2018. The M7 2016
 Kumamoto, Japan, Earthquake: 3-D Deformation Along the Fault and Within the
 Damage Zone Constrained From Differential Lidar Topography. *J. Geophys. Res. Solid*
Earth 123, 6138–6155. <https://doi.org/10.1029/2018JB015581>
 Smith, B., Sandwell, D., 2003. Coulomb stress accumulation along the San Andreas Fault
 system: COULOMB STRESS ALONG THE SAN ANDREAS FAULT. *J. Geophys. Res.*
Solid Earth 108. <https://doi.org/10.1029/2002JB002136>
 Sudhaus, H., Sigurjón, J., 2009. Improved source modelling through combined use of InSAR and
 GPS under consideration of correlated data errors: application to the June 2000
 Kleifarvatn earthquake, Iceland. *Geophys. J. Int.* 176, 389–404.
<https://doi.org/10.1111/j.1365-246X.2008.03989.x>
 ten Brink, U., 2004. Stress interaction between subduction earthquakes and forearc strike-slip
 faults: Modeling and application to the northern Caribbean plate boundary. *J. Geophys.*
Res. 109. <https://doi.org/10.1029/2004JB003031>

655 Timofeev, V.Yu., Ardyukov, D.G., Solov'ev, V.M., Shibaev, S.V., Petrov, A.F., Gornov, P.Yu.,
 656 Shestakov, N.V., Boiko, E.V., Timofeev, A.V., 2012. Plate boundaries in the Far East
 657 region of Russia (from GPS measurement, seismic-prospecting, and seismological data).
 658 Russ. Geol. Geophys. 53, 376–391. <https://doi.org/10.1016/j.rgg.2012.03.002>
 659 Tong, X., Sandwell, D., Luttrell, K., Brooks, B., Bevis, M., Shimada, M., Foster, J., Smalley, R.,
 660 Parra, H., Báez Soto, J.C., Blanco, M., Kendrick, E., Genrich, J., Caccamise, D.J., 2010.
 661 The 2010 Maule, Chile earthquake: Downdip rupture limit revealed by space geodesy:
 662 DOWNDIP RUPTURE MAULE, CHILE EARTHQUAKE. Geophys. Res. Lett. 37, n/a-
 663 n/a. <https://doi.org/10.1029/2010GL045805>
 664 Wells, D.L., Coppersmith, K.J., 1994. New empirical relationships among magnitude, rupture
 665 length, rupture width, rupture area, and surface displacement. Bull. Seismol. Soc. Am.
 666 84, 974–1002.
 667 Wright, T.J., Lu, Z., Wicks, C., 2003. Source model for the Mw 6.7, 23 October 2002, Nenana
 668 Mountain Earthquake (Alaska) from InSAR. Geophys. Res. Lett. 30.
 669 <https://doi.org/10.1029/2003GL018014>
 670 Wyss, M., Wiemer, S., 2000. Change in the Probability for Earthquakes in Southern California
 671 Due to the Landers Magnitude 7.3 Earthquake. Science 290, 1334–1338.
 672 <https://doi.org/10.1126/science.290.5495.1334>
 673 Xu, C., Liu, Y., Wen, Y., Wang, R., 2010. Coseismic Slip Distribution of the 2008 Mw 7.9
 674 Wenchuan Earthquake from Joint Inversion of GPS and InSAR Data Coseismic Slip
 675 Distribution of the Wenchuan Earthquake from Joint Inversion of GPS and InSAR Data.
 676 Bull. Seismol. Soc. Am. 100, 2736–2749. <https://doi.org/10.1785/0120090253>

677

678

679

680

681

682

683

684

685

686

687

688

689

690

691

692

693

694

695

696

697

698

699

700 **Full mailing address for each author:**

701 Magdalena Stefanova Vassileva - magdalena.stefanova.vassileva@gfz-potsdam.de - German
702 Research Centre for Geosciences, Remote Sensing, Telegrafenberg 34, 14473 Potsdam Germany
703

704 Mahdi Motagh - mahdi.motagh@gfz-potsdam.de - German Research Centre for Geosciences,
705 Remote Sensing, Telegrafenberg 34, 14473 Potsdam Germany
706

707 Thomas R. Walter - thomas.walter@gfz-potsdam.de - German Research Centre for Geosciences,
708 Physics of Earthquakes and Volcanoes, Helmholtzstraße 6/7, 14467 Potsdam, Germany
709

710 Hans-Ulrich Wetzel - hans-ulrich.wetzel@gfz-potsdam.de - German Research Centre for
711 Geosciences, Remote Sensing, Telegrafenberg 34, 14473 Potsdam Germany
712

713 Sergey L. Senyukov - ssl@emsd.ru - Kamchatkan Branch of Geophysical Survey, Russian
714 Academy of Sciences, Piipa boulevard, 9, 683006 Petropavlovsk-Kamchatskii, Russia
715

716

717

718

719

720

721

722

723

724 **List of Figure Captions**

Figure 1: Overview depicting the main geographic and geological features and tectonic complexities of Kamchatka Peninsula. Tectonic edges are represented by thick white lines; the main fault systems are represented by polyline segments: thin and lighter color for the East Kamchatka Fault Zone (EKFZ) and thin and black color for the thrust fault system of the Kumroch thrust belt (KT). Dash and dot polygon shows the Central Kamchatka Depression (CKS) zone; lighter dashed polygons represent the rupture zones of the larger historical earthquakes (Bürgmann et al., 2005; Johnson and Satake, 1999). The location of the 29 March 2017 Yuzhno-Ozernovskoe earthquake is symbolized by a star; black diamond symbolizes the locations of the main historical earthquakes discussed in the text. Natural Earth image is used as background (see Data and Resources)

Figure 2: Spatial and temporal coverage of the SAR scenes used in the co-seismic DInSAR analysis and the seismic sequence following the 29 March 6.6 Mw earthquake are shown (data from the Seismological Data Information System of Kamchatka Branch of Geophysical Survey of Russian Academy of Science Earthquakes Catalogue for Kamchatka and the Commander Islands (1962–present) (SDIS KB GS RAS); a) SAR image footprints: ALOS-2 ascending (light dot lines), ALOS-2 descending (dark dash and dot lines) and Sentinel-1A (light solid line); polyline segments show: in thin and lighter color the East Kamchatka Fault Zone (EKFZ) after (Kozhurin et al., 2006; Kozhurin and Zelenin, 2017) and in thin and black color the Kumroch thrust belt (KT); black triangles show the location of the seismic stations (see Data and

Resources); white star shows the 29 March 6.6 Mw earthquake; the scaled by magnitude stars symbolize the after-shocks; Natural Earth image is used as background (see Data and Resources); b) the seismic sequence in time domain is shown; sized and scaled stars emphasize the magnitude; lines shows the SAR temporal baselinesfor : ALOS-2 ascending (dot lines), ALOS-2 descending (dash and dot lines) and Sentinel-1A (solid line)

725 Figure 3: Comparison of the source parameters derived from the DInSAR geodetic modelling
 726 and the local and global seismological centres. The SDIS KB GS RAS (Seismological Data
 727 Information System of Kamchatka Branch of Geophysical Survey of Russian Academy of
 728 Science) Earthquakes Catalogue for Kamchatka and the Commander Islands (1962–present),
 729 focal mechanism solution as in (Chebrov et al., 2017); the GCMT (Global Centroid Moment
 730 Tensor Catalog); the USGS (United States Geological Survey); the GEOPHON
 731 (GEOForschungsNetz); the INGV (National Institute of Geophysics and Volcanology); and the
 732 GEOSCOPE (Global Network of Broadband Seismic Stations). Location uncertainty (ΔL) and
 733 depth uncertainty (ΔD) uncertainties are shown. The (*) sign labels the seismological centers that
 734 provide centroid source location (Geodetic Model, GCMT, USGS and GEOSCOPE); the not
 735 labeled seismological centers provide the hypocentre/epicentre of the earthquake (SDIS KB GS
 736 RAS, GEOFON and ING);

Figure 4: SAR Interferometric images showing the co-seismic displacement; each 2π cycle (“fringe”) corresponds to the displacement (d) of half the wavelength of the radar signal in the line-of-sight direction $\Delta\phi = 4\pi * d/\lambda$: a) ALOS-2 ascending ($\lambda/2 = 12$ cm); b) ALOS-2 descending ($\lambda/2 = 12$ cm) and c) Sentinel-1 descending ($\lambda/2 = 2.8$ cm). Reference point used to transform the phase-wrapped displacement into absolute values is symbolized by black cross

737 Figure 5: From top to bottom, ground displacement observed along the line-of-sight, model-
738 predicted displacement of best-fit slip-fault-plane solutions from the non-linear inversion
739 projected in line-of-sight direction and respective residuals for: column a) ALOS-2 ascending,
740 column b) ALOS-2 descending and column c) Sentinel-1 descending datasets

741 Figure 6: a) Uncertainty analysis for the non-linear inversion by performing 120 independent
742 optimizations with added to the data correlated noise: standard deviations and parameter trade-
743 off are shown; b) slip distribution estimated from the linear inversion: the image shows the
744 hanging wall relative to the footwall); slip magnitude is expressed by color scale; c) slip
745 distribution variance values; d) fault model plane projected on the ground; star symbols show the
746 epicenter/centroid locations from the different seismic and geodetic solutions (see Data and
747 Resources); the main local fault system is shown by black lines; surface projection of the fault
748 model is shown by light dotted line

Figure 7: Conceptual draw of the geodynamic interpretation of the 29th March 2017 earthquake
fault model (not to scale)

749

Table

Table 1: Interferometric SAR pairs

mission	band	Acquisition mode	Path and Frame	orbit path	acquisition date (DD/MM/YYYY)	normal baseline (m)	temporal baseline (days)	Incidence angle
ALOS-2	L (24cm)	Stripmap/Fine	109 - 1130	Asc.	19/01/2017 04/01/2018	47	350	41°
ALOS-2	L (24cm)	Stripmap/ Fine	9 - 2460	Desc.	06/03/2017 01/05/ 2017	118	56	31°
Sentinel-1A	C (5.6cm)	TOPSAR	89 - 404	Desc.	17/03/2017 29/03/2017	76	12	42°

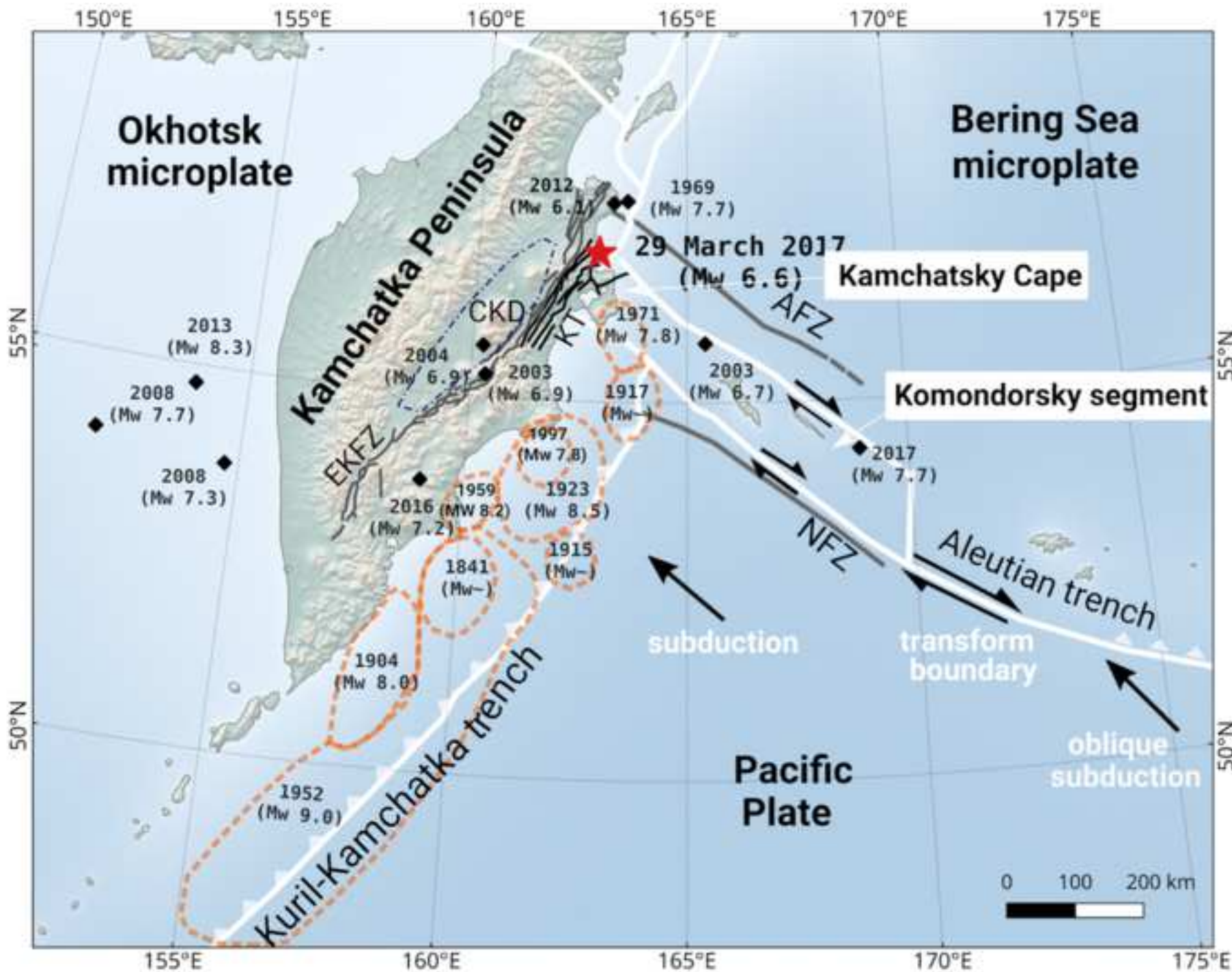
Main characteristics of the SAR scenes used in the current co-seismic displacement analysis

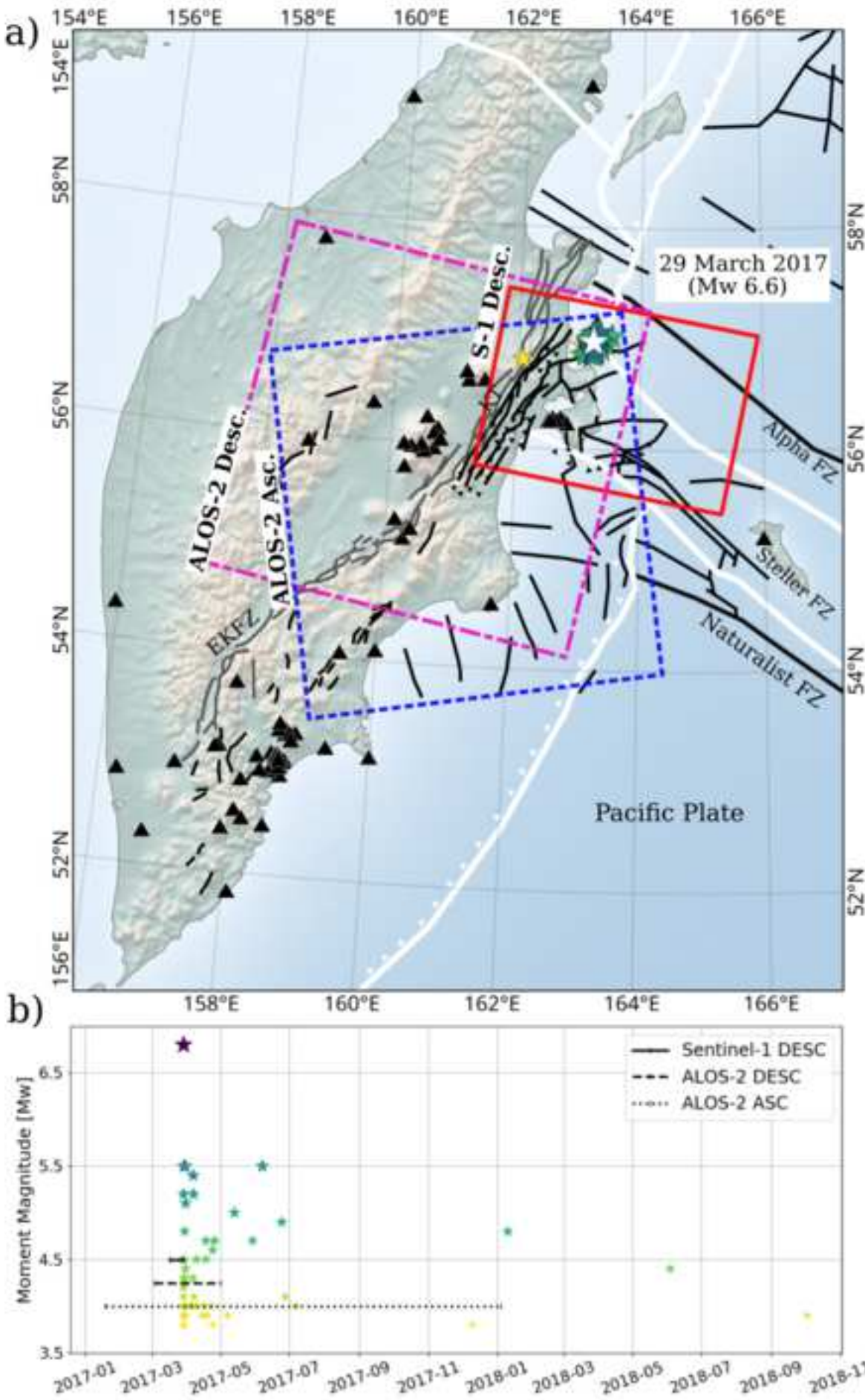
Table 2: Fault Model Parameters and Uncertainty

	E (km)	N (km)	D (km)	L (km)	W (km)	Dip (°)	Strike (°)	Rake (°)	Slip (m)
<i>Best-fit</i>	372.3	6315.5	8.1	12.9	9.1	72	213	109	2.5
St. Dev	0.8	1.0	0.8	2.4	2.3	5	12	8	0.4
Mean	372.3	6315.5	7.9	13.4	9.2	72	211	110	2.6

Geodetic fault model parameters of best-fit uniform slip-fault-plane solution derived from the non-linear optimization problem. Following standard deviation and mean values; the East and North coordinates (projected coordinate system WGS84/UTM 58N) refer to the source center, vertically projected on the surface

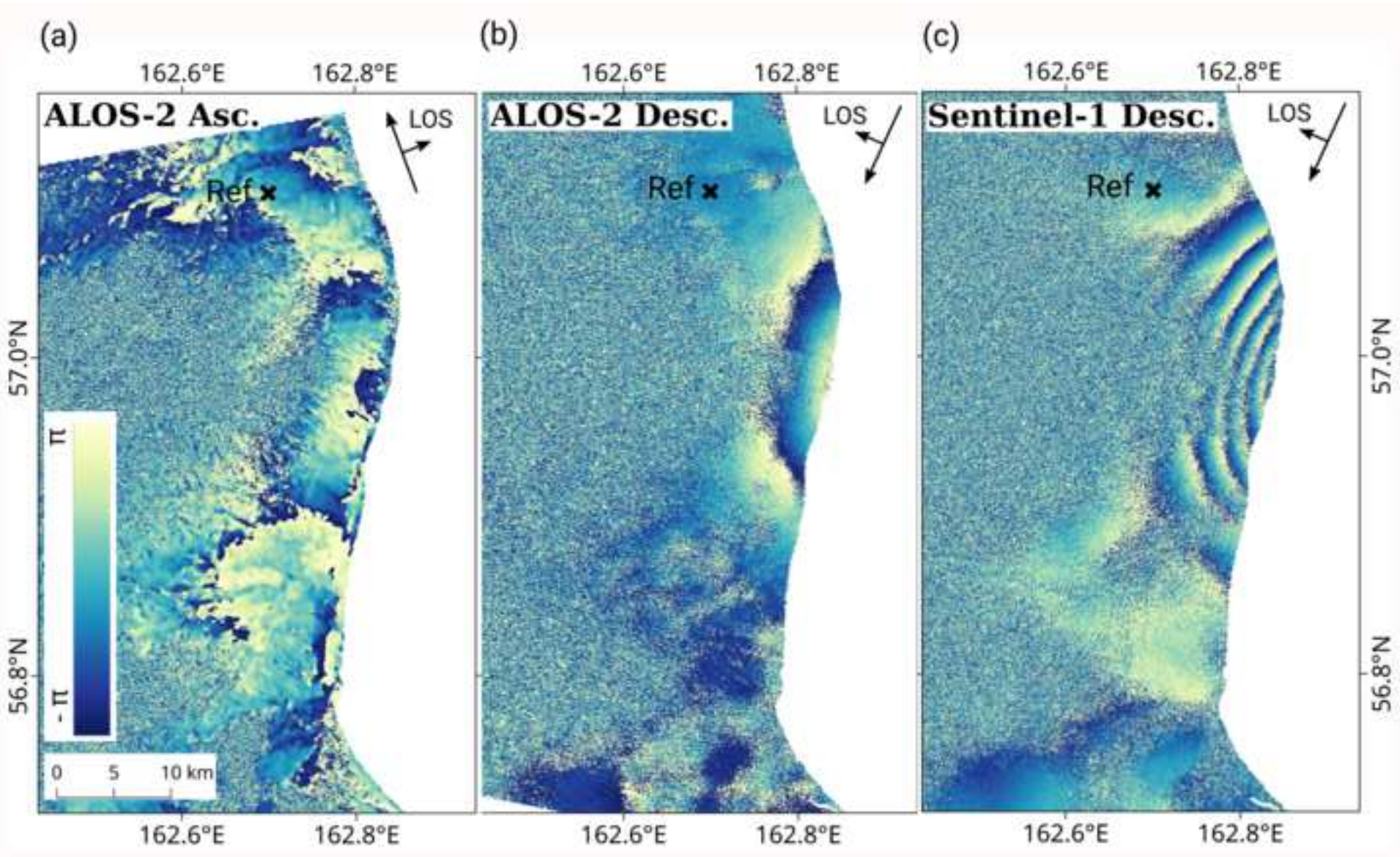
Figure1.png





[illegible]

Figure4.tif



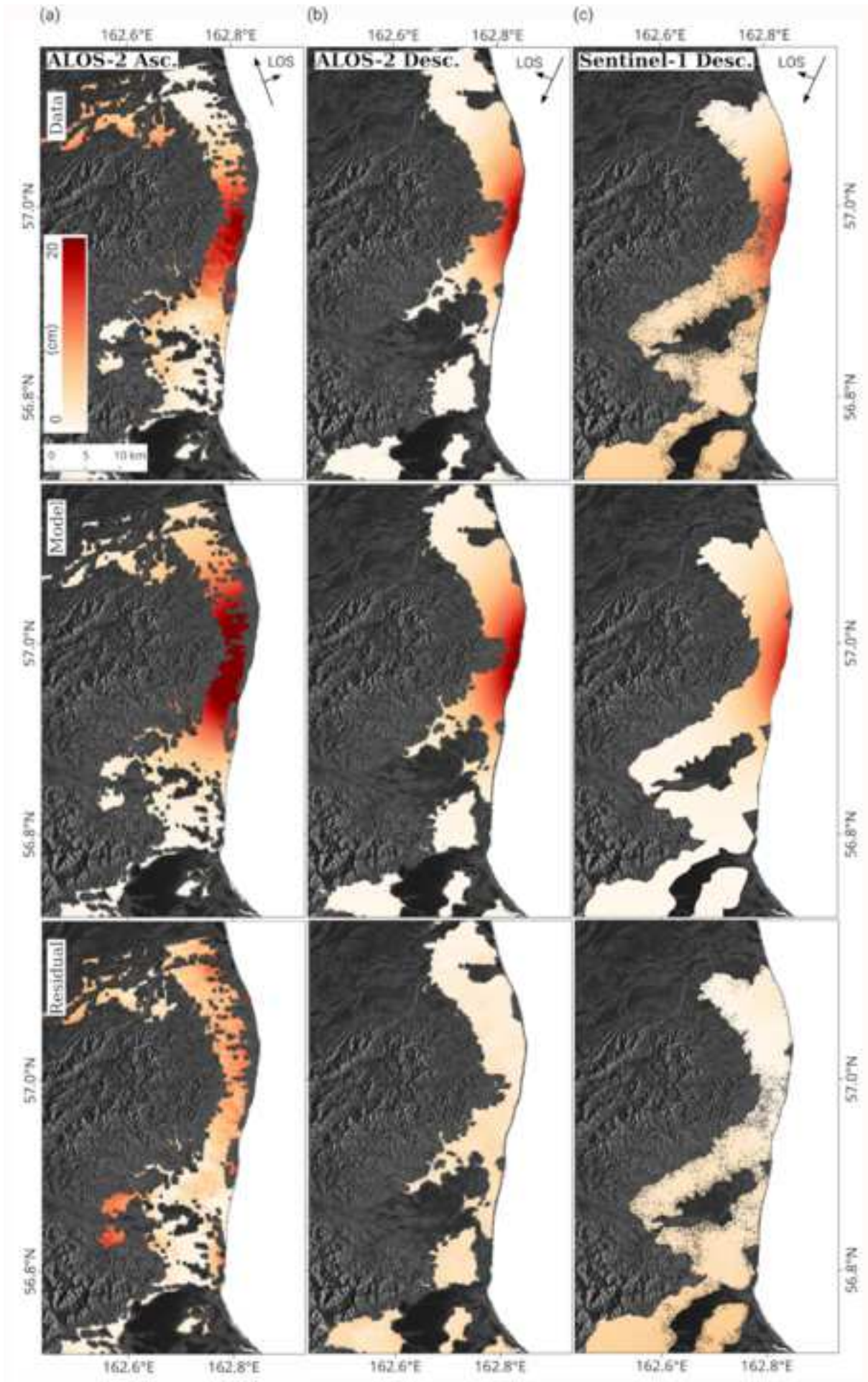


Figure6.tif

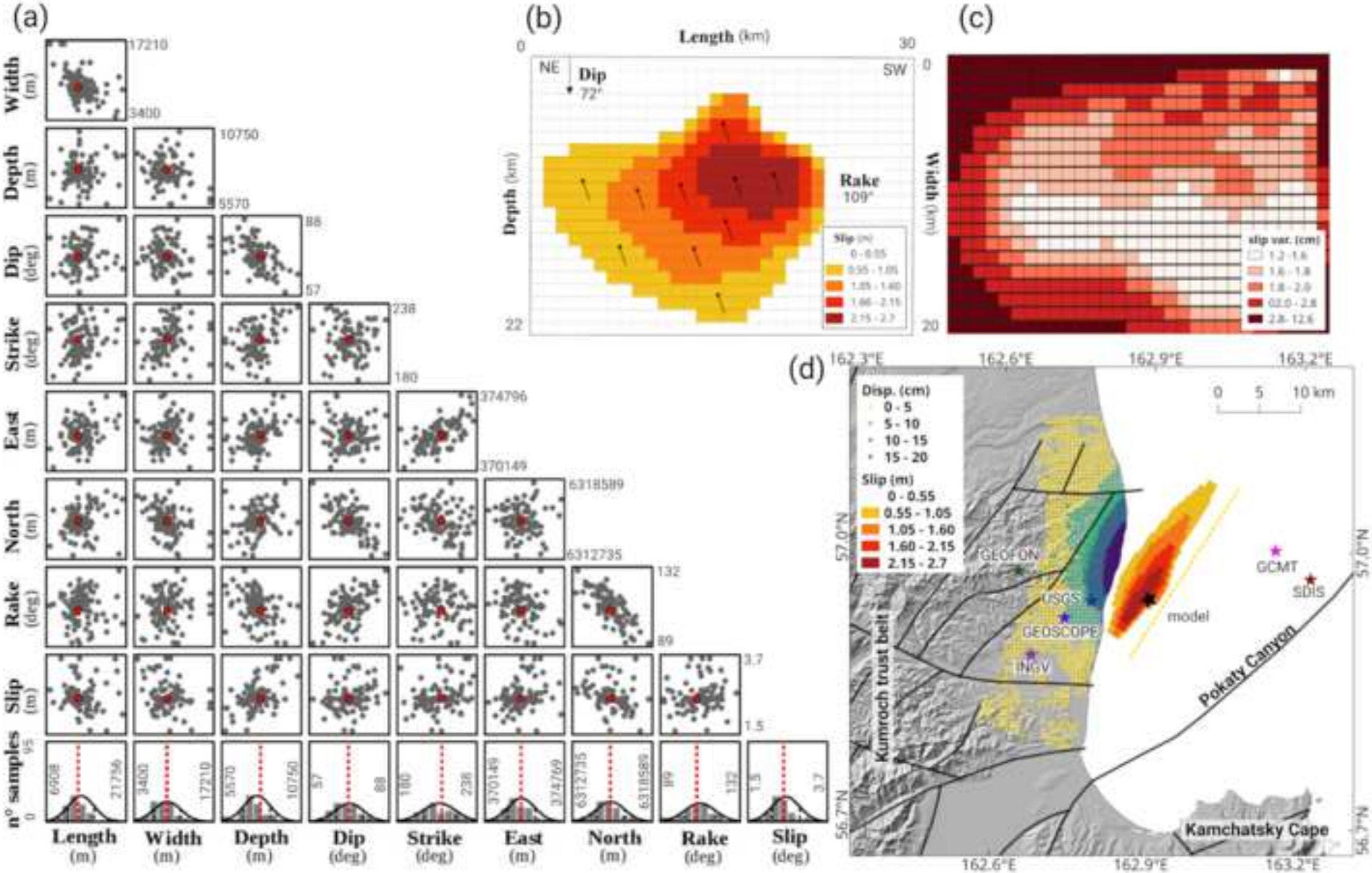


Figure7

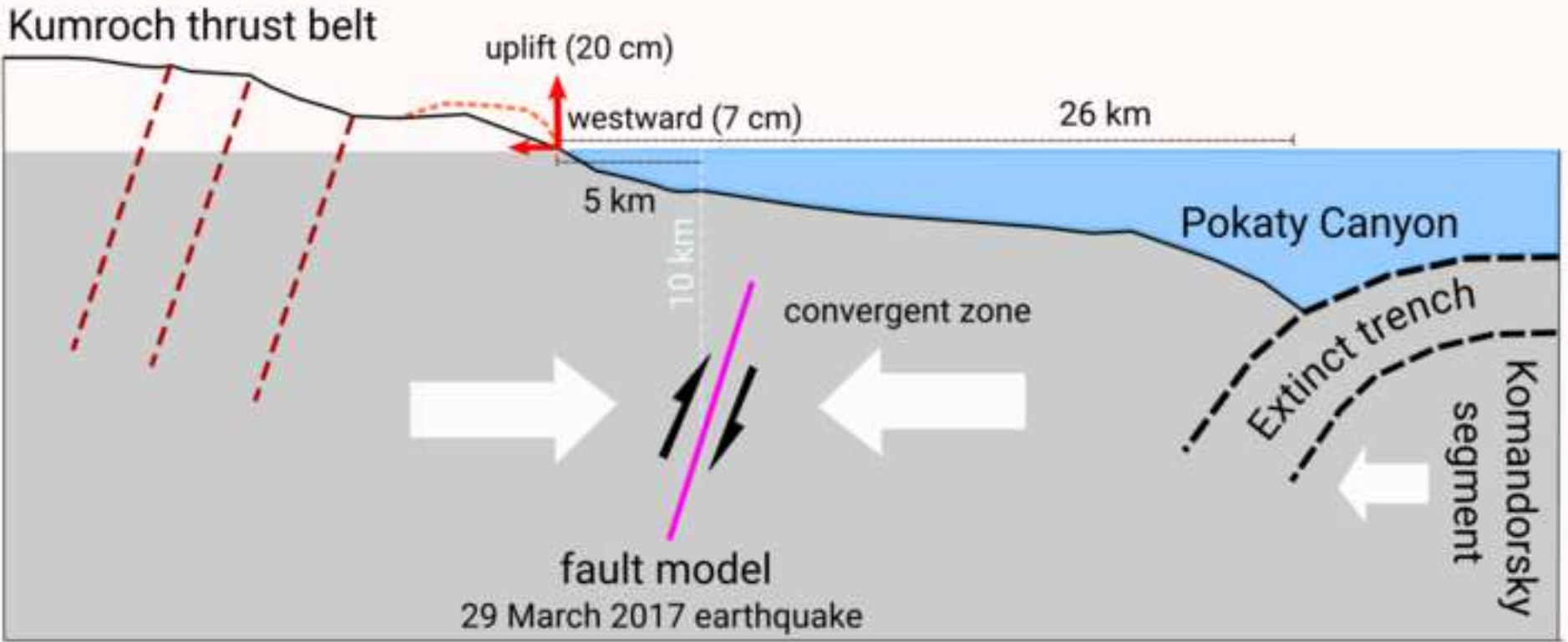


Figure7.png

Electronic supplement to

The 29 March 2017 Yuzhno-Ozernovskoe Kamchatka earthquake: fault activity in an extension of the East Kamchatka Fault Zone as constrained by InSAR observations

Magdalena S. Vassileva, Mahdi Motagh, Thomas R. Walter, Hans-Ulrich Wetzels, Sergey L. Senyukov

Description:

This electronic supplement contains three additional figures. Figure S1 shows detailed reconstruction of the tectonic setting, faulting system and main geological units of Kamchatka region, and should be consulted together with Figure 1. Figure S2 shows the 2D displacement decomposition and after-shock residuals, and it is supplementary information to Figure 4. Figure S3 shows a detailed view of Figure S1 over a restricted to the the 29 March 2017 Yuzhno-Ozernovskoe Kamchatka earthquake region, with added the seismic data and the fault model horizontal projection, which help to contextualize the event and provide the geodynamic interpretation. This final figure is supplementary to Figure 6.

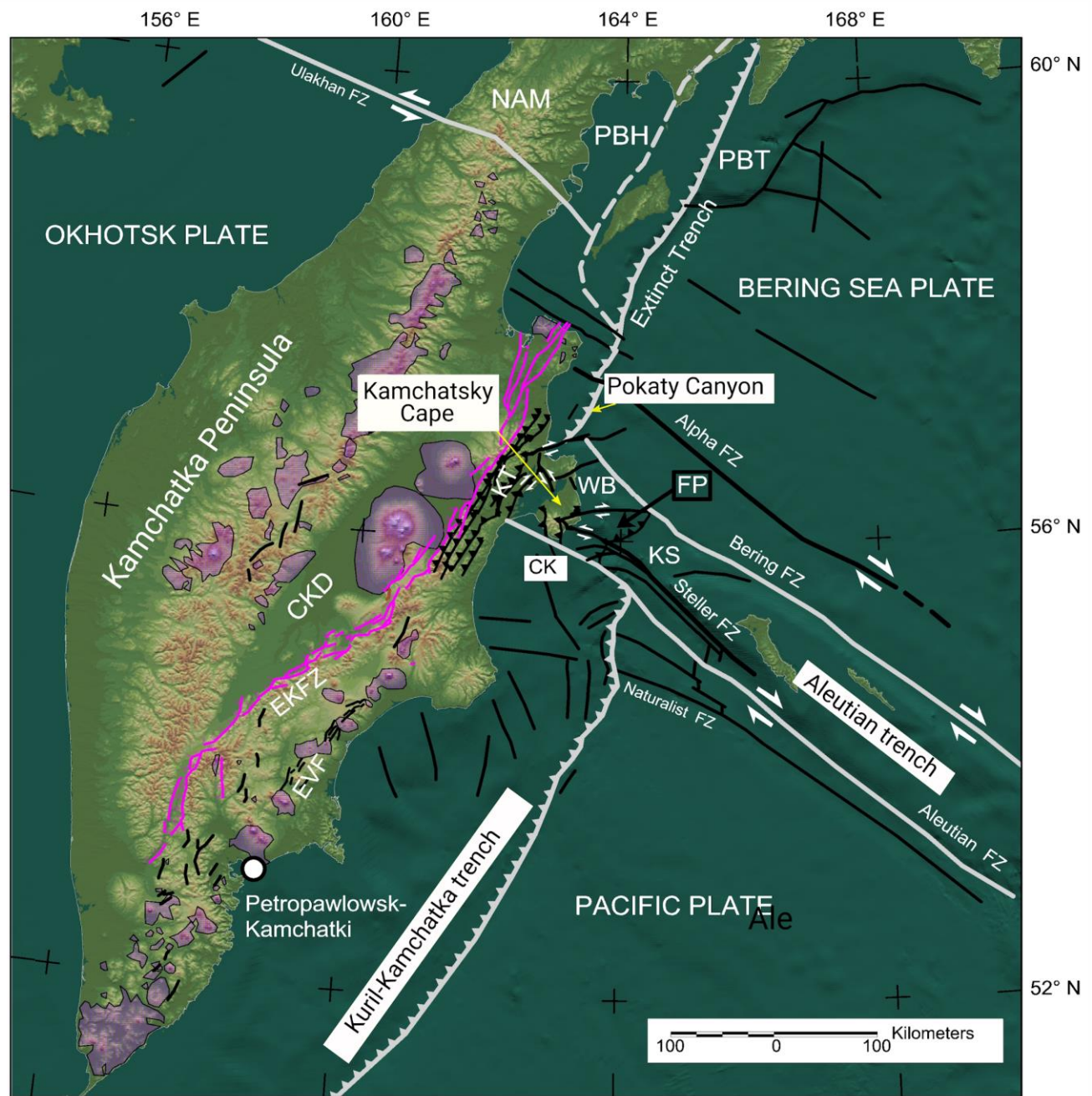


Figure S1: Central Kamchatka Depression (CKD), Komandorsky segment (KS) - frontal block of Komandorsky segment (FP), western block of Kamchatka Peninsula (WB), Ulakhasn Fault after (Hindle et al., 2019), North American Plate (NAM), Plate Boundary (PBT) after (Timofeev et al., 2012), Plate Boundary (PBH) after (Hindle et al., 2019); bathymetry from the General Bathymetric

Chart of the Oceans (see Data and Sources). Polygon areas shows the Pleistocene-Holocene volcanic and deposit units (Ponomareva et al., 2007)

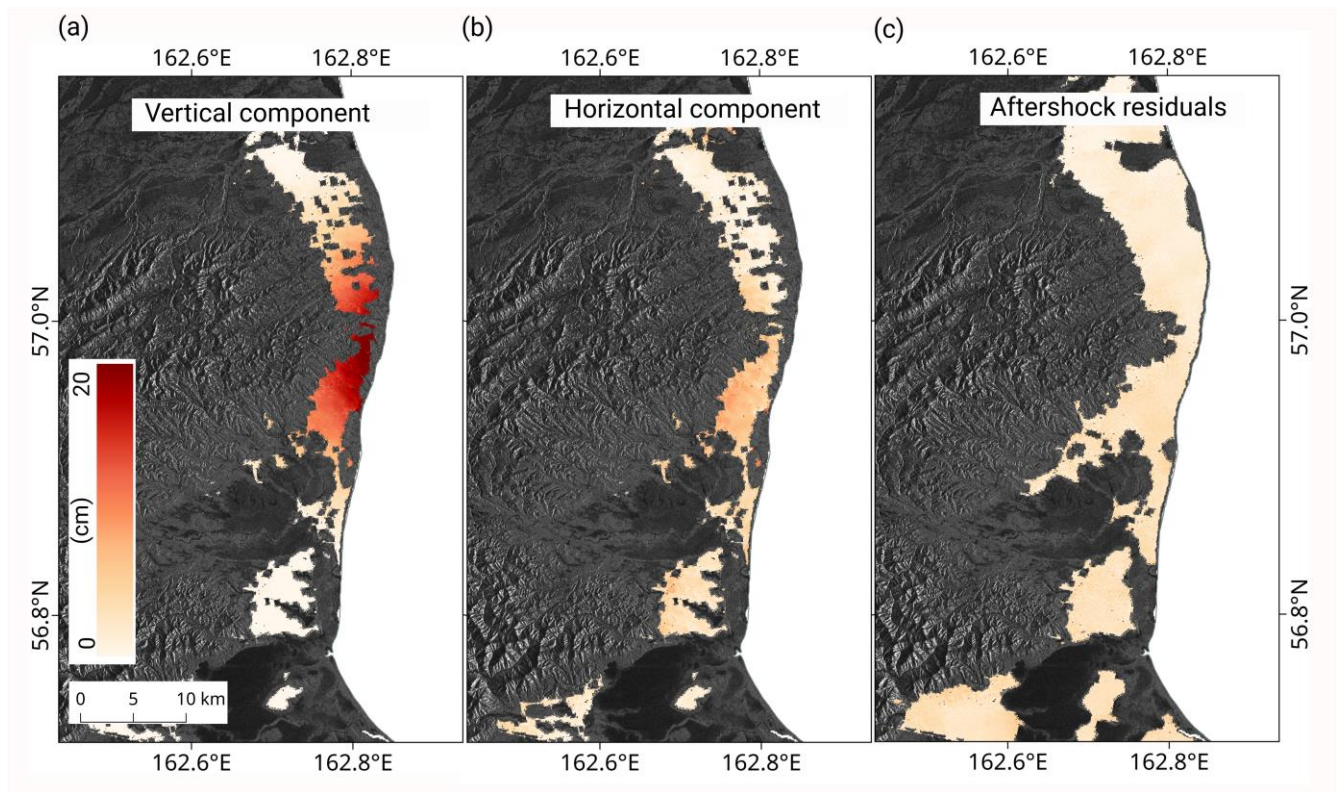


Figure S2: 2D displacement decomposition a) vertical and b) horizontal (positive values indicate westward motion); c) aftershock displacement residual between two DInSAR analysis processed using two independent descending ALOS-2 pairs: 06/032017-01/05/2017 and 27/06/2016-26/06/2017 (see Data and Resources)

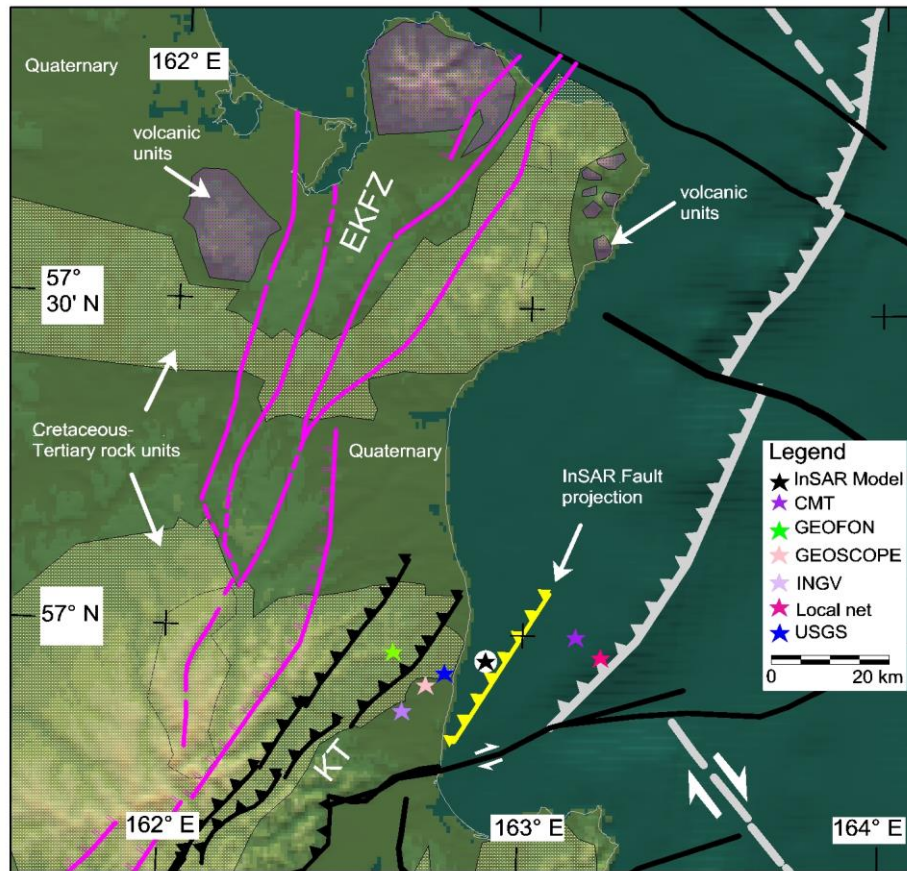


Figure S3: Detailed map over the area of interest showing the main geological units and faults: East Kamchatka Fault Zone (EKFZ) after (Kozhurin et al., 2006; Kozhurin and Zelenin, 2017) and Kumroch thrust belt (KT); star symbols shown the seismic source location according to the global and local seismological centres (see Data and Resources); black star in white circle indicates the centroid according to our geodetic fault model

Data and Resources

General Bathymetric Chart of the Oceans (GEBCO) was searched using www.gebco.net (last access June, 2019).

ALOS-2 data is a copyright of Japanese Aerospace agency and were provided under proposal 1162.

The Global Centroid Moment Tensor Project (GCMT) database was searched using <https://www.globalcmt.org/CMTsearch.html> (last accessed in June, 2019). United States Geological Survey (USGS) database was searched using <https://earthquake.usgs.gov/earthquakes/browse/> (last accessed in June, 2019). The GEOForschungsNetz (GEOFON) database was searched using <https://geofon.gfz-potsdam.de/eqinfo/form.php> (last accessed on June, 2019). The Global Network of Broad Band Seismic Stations (GEOSCOPE) was searched using <http://geoscope.ipgp.fr/index.php/en/> (last accessed in June, 2019). The National Institute of Geophysics and Volcanology (INGV) was searched using <http://cnt.rm.ingv.it/> (last accessed in June, 2019). The Seismological Data Information System of Kamchatka Branch of Geophysical Survey of Russian Academy of Science Earthquakes Catalogue for Kamchatka and the Commander Islands (1962–present) (SDIS - KB GS RAS) database was searched using <http://sdis.emsd.ru/info/earthquakes/catalogue.php> (last accessed in June, 2019).

References

- Hindle, D., Sedov, B., Lindauer, S., Mackey, K., 2019. The Ulakhan fault surface rupture and the seismicity of the Okhotsk–North America plate boundary. *Solid Earth* 10, 561–580.
<https://doi.org/10.5194/se-10-561-2019>
- Kozhurin, A., Acocella, V., Kyle, P.R., Lagmay, F.M., Melekestsev, I.V., Ponomareva, V., Rust, D., Tibaldi, A., Tunesi, A., Corazzato, C., Rovida, A., Sakharov, A., Tengonciang, A., Uy, H., 2006. Trenching studies of active faults in Kamchatka, eastern Russia: Palaeoseismic, tectonic and hazard implications. *Tectonophysics* 417, 285–304. <https://doi.org/10.1016/j.tecto.2006.01.004>
- Kozhurin, A., Zelenin, E., 2017. An extending island arc: The case of Kamchatka. *Tectonophysics* 706–707, 91–102. <https://doi.org/10.1016/j.tecto.2017.04.001>
- Ponomareva, V., Melekestsev, I., Braitseva, O., Churikova, T., Pevzner, M., Sulerzhitsky, L., 2007. Late Pleistocene-Holocene volcanism on the Kamchatka Peninsula, Northwest Pacific Region, in: Eichelberger, J., Gordeev, E., Izbekov, P., Kasahara, M., Lees, J. (Eds.), *Geophysical*

Monograph Series. American Geophysical Union, Washington, D. C., pp. 165–198.

<https://doi.org/10.1029/172GM15>

Timofeev, V.Yu., Ardyukov, D.G., Solov'ev, V.M., Shibaev, S.V., Petrov, A.F., Gornov, P.Yu.,

Shestakov, N.V., Boiko, E.V., Timofeev, A.V., 2012. Plate boundaries in the Far East region of Russia (from GPS measurement, seismic-prospecting, and seismological data). *Russ. Geol. Geophys.* 53, 376–391. <https://doi.org/10.1016/j.rgg.2012.03.002>